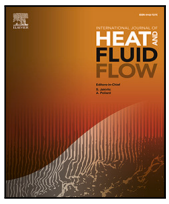
International Journal of Heat and Fluid Flow 122 (2026) 110739



Contents lists available at ScienceDirect

International Journal of Heat and Fluid Flow

journal homepage: www.elsevier.com/locate/ijhff



Critical assessment of RANS models for turbulent heat transfer in low-Prandtl-number forced convection ☆

L. Marocco [b], J. Schmitt [a], J. Neuhauser [a], B. Frohnapfel [a], D. Gatti [a,*]

[a] Karlsruhe Institute of Technology, Institute of Fluid Mechanics, Kaiserstr. 10, Karlsruhe, Germany
[b] Politecnico di Milano, Department of Energy, via Lambruschini 4, Milano, Italy

ARTICLE INFO

Keywords:
RANS
Liquid metals
Low-Prandtl-number flows
Turbulent heat transfer
Reproducibility
Numerical robustness

ABSTRACT

Reliable modeling of turbulent heat transfer in liquid metals via Reynolds–Averaged Navier–Stokes (RANS) remains challenging because the very low Prandtl number weakens the similarity between momentum and thermal transport. In this work, several thermal turbulence closures for forced convection in liquid metals are assessed using the finite-volume code OpenFOAM v2212. The investigated model combinations include the k–ω SST model with the Kays correlation for the turbulent Prandtl number, the four-equation k–ε–k_θ–ε_θ model, the logarithmic k–Ω–k_θ–Ω_θ model, and two algebraic heat-flux formulations coupled with either a low-Reynolds k–ε model or an elliptic blending Reynolds-stress model (EBRSM). The models are evaluated in turbulent channel flow, pipe flow, and heated backward-facing step flow against direct numerical simulation data and reference results reported in the original model publications, with particular attention to reproducibility, numerical robustness, and predictive accuracy.

The results show that only a limited subset of models can be considered reliable for low-Prandtl-number flows. The k–ω SST combined with the Kays correlation provides the most robust overall performance and accurate temperature predictions in all cases. The k–ε–k_θ–ε_θ model also shows good reproducibility and satisfactory agreement with reference data, remaining the most consistent multi-equation alternative. In contrast, the logarithmic four-equation model exhibits reduced numerical robustness, while the algebraic heat-flux model coupled with the k–ε momentum closure fails to reproduce published thermal results despite correct prediction of the momentum field. The EBRSM-based algebraic heat-flux formulation reproduces selected reference results but suffers from significant robustness limitations. The study establishes a unified formulation of the examined closures by reconciling discrepancies and correcting inconsistencies in their published formulations, and systematically verifies their reproducibility and robustness in low-Prandtl-number forced convection.

1. Introduction

The increasing demand for efficient thermal management in advanced energy systems has renewed interest in liquid metals as heat transfer fluids. The ratio between momentum and thermal diffusivity, the so-called Prandtl number (Pr), is in the range 10^{-3}–10^{-2} for liquid metals and thus very small, thus decoupling momentum and thermal transport (Grötzbach, 2013; Straub et al., 2019; Marocco et al., 2016). As a consequence, standard turbulence modeling assumptions, such as the similarity between velocity and temperature fields and the use of a constant turbulent Prandtl number, become questionable (Mathur et al., 2023).

In the Reynolds-Averaged Navier—Stokes (RANS) framework, turbulent heat transfer is modeled through two distinct components: a momentum turbulence model, which provides the Reynolds stresses, either through the Boussinesq hypothesis in terms of a turbulent viscosity or via Reynolds-stress transport equations, and a thermal turbulence model, which determines the turbulent heat flux through an appropriate closure.

Momentum turbulence models are independent of the fluid Pr number. The most commonly adopted formulations for momentum turbulence modeling are based on high-Reynolds-number k–ε models with wall functions, as well as low-Reynolds-number models of the k–ω family, in particular the widely used k–ω SST model (Menter et al., 2003). More advanced closures include low-Reynolds-number formulations such as the k–ε models of Abe et al. (1994) and Lien et al. (1996), and Reynolds-stress models such as the elliptic blending Reynolds-stress

☆ This article is part of a Special issue entitled: 'ETMM15' published in International Journal of Heat and Fluid Flow.

* Corresponding author.
E-mail address: davide.gatti@kit.edu (D. Gatti).

https://doi.org/10.1016/j.ijheatfluidflow.2026.110739
Received 4 May 2026; Received in revised form 20 July 2026; Accepted 2 October 2026
Available online 22 October 2026
0142-727X/© 2026 The Authors. Published by Elsevier Inc. This is an open access article under the CC BY license (http://creativecommons.org/licenses/by/4.0/).
Open access funding enabled and organized by Projekt DEAL.

Nomenclature

Roman letters

c_f	Skin-friction coefficient
c_p	Specific heat capacity at constant pressure
d_w	Distance to the nearest wall
D	Pipe diameter
ER	Expansion ratio of the backward-facing step
k	Turbulent kinetic energy
l_{step}	Backward-facing step height
k_θ	Half temperature variance
Nu_x	Local Nusselt number
p	Pressure
P_k	Production of turbulent kinetic energy
P_θ	Thermal production term
Pr	Prandtl number
Pr_t	Turbulent Prandtl number
q_w	Wall heat flux
R	Time-scale ratio
Re	Reynolds number
Re_b	Bulk Reynolds number
Re_τ	Friction Reynolds number
T	Temperature
T_{ref}	Reference temperature
T_τ	Friction temperature
u_i	Velocity components in Cartesian coordinates
u_b	Bulk velocity
u_τ	Friction velocity
x, y, z	Cartesian coordinates

Greek letters

α	Thermal diffusivity
α_t	Turbulent thermal diffusivity
δ	Channel half-height
δ_{ij}	Kronecker delta
ε	Pseudo dissipation rate of k
ε_θ	Dissipation rate of k_θ
θ	Temperature variable
λ	Thermal conductivity
ν	Kinematic viscosity
ν_t	Turbulent viscosity
ρ	Density
τ_w	Wall shear stress
Ω	Logarithmic form of ω
Ω_θ	Logarithmic form of ω_θ
ω	Specific dissipation rate of k
ω_θ	Specific dissipation rate of k_θ

Operators

$(\cdot)'$	Fluctuating quantity
$(\cdot)^+$	Quantity scaled in wall units

Acronyms

AHFM	Algebraic Heat Flux Model
BFS	Backward-Facing Step
EBRSM	Elliptic Blending Reynolds-Stress Model
RANS	Reynolds-averaged Navier–Stokes
SGDH	Simple Gradient Diffusion Hypothesis

model (EBRSM) of Lardeau and Manceau (2014). These models provide the turbulent viscosity and constitute the basis for the momentum turbulence component of all model combinations investigated in the present study.

In contrast, thermal turbulence models are directly affected by the Prandtl number, as they govern the relationship between momentum and thermal transport. Most available thermal closures have been originally developed for fluids with $Pr \approx 1$, where the analogy between velocity and temperature fields is reasonably valid. This includes temperature-variance-based models derived from the work of Abe et al. (1995) and algebraic heat-flux formulations based on Kenjeres et al. (2005).

Extensions of these models to low-Prandtl-number flows have been proposed through modified formulations, additional terms, or empirical corrections. However, these extensions are not uniquely defined and often differ across publications, leading to ambiguities in the mathematical formulation and difficulties in reproducing published results. As a consequence, discrepancies between different studies are frequently observed, even when nominally the same model is employed.

Within this context, the present work focuses on a set of thermal turbulence closures that have been widely adopted and further developed for low-Prandtl-number flows. These include multi-equation models based on temperature variance transport, such as the four-equation k–ε–k_θ–ε_θ model proposed by Manservisi and Menghini (2014a) and the logarithmic k–Ω–k_θ–Ω_θ model introduced by Da Vià et al. (2016), both derived from the original formulations of Abe et al. (1995). In addition, algebraic heat-flux models (AHFM), such as those proposed by Shams et al. (2014), are considered. These models are based on the formulation of Kenjeres et al. (2005) and have been extended to liquid-metal flows and coupled with different momentum turbulence models, including low-Reynolds-number closures derived from Lien et al. (1996) and Reynolds-stress models such as the EBRSM of Lardeau and Manceau (2014).

A simpler alternative consists in modeling the turbulent heat flux through a turbulent Prandtl number, as in the correlation proposed by Kays (1994), here coupled with a k–ω SST momentum turbulence model (Menter et al., 2003). This approach provides a local relation between turbulent viscosity and thermal diffusivity. While computationally efficient, it remains empirical and its validity in low-Prandtl-number flows is not guaranteed a priori.

The present study addresses these issues through a systematic assessment of RANS turbulence models for forced convection in liquid metals with three main objectives: (i) to reconstruct and verify the mathematical formulation of selected momentum and thermal turbulence models by resolving discrepancies, ambiguities, and inconsistencies found in their original publications, (ii) to assess the reproducibility of reference results reported by the model developers, and (iii) to evaluate model accuracy against high-fidelity data, including direct numerical simulation (DNS) and large-eddy simulation (LES). To the authors' knowledge, these aspects have not been addressed simultaneously in a unified framework for low-Prandtl-number flows. The assessment deliberately targets the low-Prandtl-number regime ($Pr \leq 0.025$) for which the considered closures and their coefficients were calibrated; their parent formulations for $Pr \approx 1$ fluids have been extensively validated in the original publications (Abe et al., 1995; Kenjeres et al., 2005; Kays, 1994).

The model families considered in this work have been selected based on their widespread use and continued development in the literature (Roelofs, 2020). However, as detailed in Section 2, the specific published forms of these models contain discrepancies across publications. Reconstructing a single consistent formulation, and documenting the choices made, is one of the objectives of the present work.

The assessment is carried out on a set of canonical and complex test cases, including turbulent channel flow, pipe flow, and heated backward-facing step flow. These configurations are commonly adopted in the original model development studies. Moreover, they are standard

benchmarks in the literature and are characterized by the availability of high-fidelity reference data from DNS and LES, allowing for a systematic evaluation of predictive accuracy, numerical robustness, and reproducibility across different flow regimes and model combinations.

All models have been implemented into (and tested with) a single, finite-volume code OpenFOAM v2212 (OpenCFD Ltd, 2022), adopting a modular framework in which momentum and thermal turbulence closures are treated independently and can be combined systematically. Furthermore, the implemented models, the corresponding simulation cases, and a complete database of the obtained results are provided as accompanying material. This guarantees full reproducibility of the present study, enables consistent and unbiased comparisons across different modeling approaches, and establishes a reference dataset for future development and validation of turbulence models for low-Prandtl-number flows.

The outline of the paper is as follows. Section 2 introduces the considered turbulence models in detail, including their formulation. In Section 3, the numerical setup of the test cases is described, which are used for model assessment in Section 4 together with a discussion of the reproducibility and numerical stability for each of the models.

2. Considered turbulence models and their formulation

This section presents the turbulence models considered in the present study together with their mathematical formulation. For clarity, the models are organized according to their role in the closure of the RANS equations, distinguishing between momentum turbulence models and thermal turbulence models.

The momentum turbulence models are described first, as they provide the underlying closure for the Reynolds stresses and supply the quantities required by the thermal turbulence models. The thermal turbulence models are then introduced separately, grouped according to the type of closure adopted for the turbulent heat flux, namely turbulent-Prandtl-number, multi-equation, and algebraic heat-flux approaches.

Although thermal turbulence models depend on the underlying momentum closure, this separation provides a clearer presentation of the model hierarchy and of the specific role of each component. Their actual coupling in the simulations is defined through the model combinations summarized in Table 1 and discussed in Section 2.1.

2.1. Model selection

The turbulence model combinations considered in this study are summarized in Table 1. They are representative of the most widely adopted approaches for modeling turbulent heat transfer in low-Pr-number flows.

Each combination consists of a momentum turbulence model and a thermal turbulence closure. For the multi-equation thermal closures, it should be noted that the thermal model is calibrated together with a specific momentum turbulence model. Therefore, combining such closures with a different momentum model generally leads to poor performance.

An alternative assessment strategy consists in combining different thermal closures with a single, reliable momentum model, which would isolate the intrinsic accuracy of the thermal closures. This approach is deliberately not pursued here: the multi-equation thermal models are calibrated jointly with their momentum closure, and departing from the published pairings would compromise the reproducibility assessment, which is the primary objective of this study. The modular framework provided as supplementary material nevertheless enables such cross-combination studies, which represent a natural extension of the present work.

The abbreviations introduced in Table 1 are used consistently throughout the paper.

Table 1
Overview of selected turbulence model combinations. The first model in each block corresponds to the momentum turbulence model, and the second represents the thermal turbulence model.

Momentum model	Thermal model	Abbreviation
k-ω SST	Kays correlation	KWSST-KAYS
k-ε (AKN)	k_θ-ε_θ (MM)	AKN-MM
k-Ω (KLW)	k_θ-Ω_θ (DAVIA)	KLW-DAVIA
k-ε (ShamsKE)	AHFM-NRG	ShamsKE-AHFM
EBRSM	AHFM-NRG	EBRSM-AHFM

2.2. Momentum turbulence models

The momentum turbulence models considered in this study are those forming the basis of the thermal turbulence closures investigated in the following.

In particular, the low-Reynolds-number k–ε model of Abe et al. (1994) (AKN) and its logarithmic reformulation as a k–Ω model proposed by Da Vià et al. (2016) (KLW) provide the underlying momentum closures for the multi-equation thermal turbulence models MM and DAVIA, respectively.

For the algebraic heat-flux approach, the AHFM closure is coupled with either the ShamsKE variant proposed by Shams et al. (2014), based on the low-Reynolds-number k–ε model of Lien et al. (1996), or with the EBRSM of Lardeau and Manceau (2014).

The k–ω SST model (Menter et al., 2003) and the EBRSM (Lardeau and Manceau, 2014; Manceau, 2015) are employed as implemented in OpenFOAM v2212 (OpenCFD Ltd, 2022). For these models, reference is made to Lardeau and Manceau (2014), Manceau (2015) and to the OpenFOAM documentation.

In the present study, the EBRSM is used as implemented in OpenFOAM v2212, following the formulation of Manceau (2015). This differs from the version considered by Shams and De Santis (2019), which is based on Lardeau and Manceau (2014). The use of different implementations of the EBRSM may therefore represent one possible source of the discrepancies observed in the present assessment.

The AKN and KLW models, and the ShamsKE formulation are described in detail in the following subsections.

2.2.1. k–ε AKN

The low-Reynolds-number k–ε model proposed by Abe et al. (1994) is used as the reference momentum turbulence model for the multi-equation thermal closures (k_θ-ε_θ and k_θ-Ω_θ) considered in this study. The model is formulated in terms of transport equations for the turbulent kinetic energy k and its pseudo-dissipation rate ε:

$$\frac{\partial k}{\partial t} + u_i \frac{\partial k}{\partial x_i} = \frac{\partial}{\partial x_i}\left[\left(\nu + \frac{\nu_t}{\sigma_k}\right)\frac{\partial k}{\partial x_i}\right] + P_k - \varepsilon \tag{1}$$

$$\frac{\partial \varepsilon}{\partial t} + u_i \frac{\partial \varepsilon}{\partial x_i} = \frac{\partial}{\partial x_i}\left[\left(\nu + \frac{\nu_t}{\sigma_\varepsilon}\right)\frac{\partial \varepsilon}{\partial x_i}\right] + C_{\varepsilon 1}\frac{\varepsilon}{k}P_k - C_{\varepsilon 2} f_\varepsilon \frac{\varepsilon^2}{k} \tag{2}$$

The production of turbulent kinetic energy is defined as

$$P_k = -\overline{u_i' u_j'}\frac{\partial u_i}{\partial x_j}, \tag{3}$$

while the Reynolds stresses $\overline{u_i' u_j'}$ are modeled using the Boussinesq hypothesis

$$\overline{u_i' u_j'} = -\nu_t\left(\frac{\partial u_i}{\partial x_j} + \frac{\partial u_j}{\partial x_i}\right) + \frac{2}{3}k\delta_{ij} \tag{4}$$

The quantity ε represents the pseudo-dissipation rate (Pope, 2000), defined as

$$\varepsilon = \nu\overline{\frac{\partial u_i'}{\partial x_j}\frac{\partial u_i'}{\partial x_j}} \tag{5}$$

Within the model, ε is obtained from its transport equation (Eq. (2)). Eq. (5) only specifies the quantity being modeled, which is relevant for

the formulation of the wall boundary condition and for the comparison with DNS data.

The turbulent viscosity is defined as

$$\nu_t = C_\mu f_\mu \frac{k^2}{\varepsilon} \tag{6}$$

The model coefficients in Eqs. (1), (2) and (6) are

$$\sigma_k = 1.4, \quad \sigma_\varepsilon = 1.4, \quad C_{\varepsilon 1} = 1.5, \quad C_{\varepsilon 2} = 1.9, \quad C_\mu = 0.09 \tag{7}$$

while the damping functions f_μ and f_ε, with which the near-wall effects are accounted for, are defined as

$$f_\mu = \left(1 - e^{-R_\delta/14}\right)^2 \left(1 + \frac{5}{R_t^{3/4}} e^{-(R_t/200)^2}\right) \tag{8}$$

$$f_\varepsilon = \left(1 - e^{-R_\delta/3.1}\right)^2 \left(1 - 0.3 e^{-(R_t/6.5)^2}\right) \tag{9}$$

Here, R_t is the turbulent Reynolds number and R_δ is the ratio of the distance to the nearest wall to the Kolmogorov length scale. They are defined as

$$R_t = \frac{k^2}{\nu\varepsilon} \qquad \text{and} \qquad R_\delta = \frac{d_w}{\left(\nu^3/\varepsilon\right)^{1/4}} \tag{10}$$

with d_w denoting the distance to the nearest wall.

In the original formulation of Abe et al. (1994), near-wall scaling is expressed in terms of wall units (y^+). In the present work, a fully local formulation based on R_t and R_δ is adopted, following Manservisi and Menghini (2014a). This avoids the explicit evaluation of wall units and ensures consistency when applying the model to complex geometries and unstructured meshes.

2.2.2. k–Ω model (KLW)

The k–Ω model was introduced by Da Vià et al. (2016) as the momentum turbulence closure within the k-Ω-k_θ-Ω_θ model combination. The model is based on the formulation of Abe et al. (1994), with the dissipation rate ε replaced by the logarithmic variable Ω, defined as:

$$\Omega = \ln(\omega) \qquad \text{where} \quad \omega = \frac{\varepsilon}{C_\mu k} \quad \text{and} \quad C_\mu = 0.09 \tag{11}$$

The use of a logarithmic transformation of the specific dissipation rate ω is intended to improve numerical robustness compared to the AKN model, as discussed by Da Vià et al. (2016). The transport equation for k is identical to Eq. (1), with the substitution $\varepsilon = C_\mu k e^\Omega$, which must also be applied in Eqs. (6) and (10).

The KLW model differs from the AKN model by solving the following transport equation for Ω instead of ε:

$$\begin{aligned}\frac{\partial \Omega}{\partial t} + u_i \frac{\partial \Omega}{\partial x_i} = \frac{\partial}{\partial x_i}\left[\left(\nu + \frac{\nu_t}{\sigma_\varepsilon}\right)\frac{\partial \Omega}{\partial x_i}\right] + \frac{2}{k}\left(\nu + \frac{\nu_t}{\sigma_\varepsilon}\right)\frac{\partial k}{\partial x_i}\frac{\partial \Omega}{\partial x_i} \\ + \left(\nu + \frac{\nu_t}{\sigma_\varepsilon}\right)\frac{\partial \Omega}{\partial x_i}\frac{\partial \Omega}{\partial x_i} + \frac{C_{\varepsilon 1} - 1}{k} P_k - C_\mu (C_{\varepsilon 2} f_\varepsilon - 1) e^\Omega\end{aligned} \tag{12}$$

The model coefficients σ_k, σ_ε, $C_{\varepsilon 1}$, and $C_{\varepsilon 2}$, as well as the damping functions f_μ and f_ε, are identical to those of the AKN model (Section 2.2.1). The second and third terms on the right-hand side of Eq. (12) correspond to cross-diffusion contributions. By introducing

$$D_1 = \frac{2}{k}\left(\nu + \frac{\nu_t}{\sigma_\varepsilon}\right), \qquad D_2 = \left(\nu + \frac{\nu_t}{\sigma_\varepsilon}\right)$$

they can be rewritten as:

$$D_1 \frac{\partial k}{\partial x_i}\frac{\partial \Omega}{\partial x_i} = \frac{\partial}{\partial x_i}\left(D_1 \frac{\partial k}{\partial x_i}\Omega\right) - \Omega \frac{\partial}{\partial x_i}\left(D_1 \frac{\partial k}{\partial x_i}\right)$$

$$D_2 \frac{\partial \Omega}{\partial x_i}\frac{\partial \Omega}{\partial x_i} = \frac{\partial}{\partial x_i}\left(D_2 \frac{\partial \Omega}{\partial x_i}\Omega\right) - \Omega \frac{\partial}{\partial x_i}\left(D_2 \frac{\partial \Omega}{\partial x_i}\right)$$

This reformulation enables a partially implicit treatment of the cross-diffusion terms. In the present implementation, both implicit and explicit treatments are supported. When the implicit option is disabled, these terms are treated as explicit source contributions.

2.2.3. Shams k–ε model (ShamsKE)

The ShamsKE model is a low-Reynolds-number turbulence model used in combination with the AHFM-NRG thermal turbulence closure (Section 2.3.4), as introduced by Shams et al. (2014). The implementation adopted in this work is based on the formulation reported by Shams et al. (2014), which itself is derived from the low-Reynolds-number k–ε model of Lien et al. (1996). Since Shams et al. (2014) do not explicitly define the dissipation rate of k, it is assumed that the pseudo-dissipation rate ε defined in Eq. (5) is employed.

The transport equations for k and ε are:

$$\frac{\partial(\rho k)}{\partial t} + u_i \frac{\partial(\rho k)}{\partial x_i} = \frac{\partial}{\partial x_i}\left[\rho\left(\nu + \frac{\nu_t}{\sigma_k}\right)\frac{\partial k}{\partial x_i}\right] + \rho P_k - \rho\varepsilon \tag{13}$$

$$\begin{aligned}\frac{\partial(\rho\varepsilon)}{\partial t} + u_i \frac{\partial(\rho\varepsilon)}{\partial x_i} = \frac{\partial}{\partial x_i}\left[\rho\left(\nu + \frac{\nu_t}{\sigma_\varepsilon}\right)\frac{\partial \varepsilon}{\partial x_i}\right] + \frac{\rho C_{\varepsilon 1}}{\tau}(P_k + P_{\text{wall}}) + \\ - \rho C_{\varepsilon 2} f_\varepsilon \frac{\varepsilon}{\tau} + \rho S_Y\end{aligned} \tag{14}$$

The production term P_k is defined in Eq. (3). The turbulent viscosity and auxiliary functions are:

$$\nu_t = C_\mu f_\mu k \tau\,, \tag{15}$$

$$f_\mu = 1 - \exp\left[-\left(C_{d_0}\sqrt{Re_d} + C_{d_1} Re_d + C_{d_2} Re_d^2\right)\right], \tag{16}$$

$$Re_d = \frac{\sqrt{k}\, d_w}{\nu}, \tag{17}$$

$$f_\varepsilon = \left(1 - C e^{-R_t^2}\right), \tag{18}$$

$$\tau = \max\left(\frac{k}{\varepsilon}, \sqrt{\frac{\nu}{\varepsilon}}\right) \tag{19}$$

where d_w denotes the distance to the nearest wall.

The near-wall production term reads

$$P_{\text{wall}} = D f_\varepsilon \left(P + 2\nu \frac{k}{d_w^2}\right) e^{-E Re_d^2}, \tag{20}$$

while the term S_Y represents the Yap correction (Yap, 1987), as adopted by Shams (2018):

$$S_Y = C_w \frac{\varepsilon}{\tau} \max\left\{\left(\frac{\hat{l}}{l_\varepsilon} - 1\right)\left(\frac{\hat{l}}{l_\varepsilon}\right)^2, 0\right\}, \quad \hat{l} = \frac{k^{3/2}}{\varepsilon}, \; l_\varepsilon = C_l d_w \tag{21}$$

Buoyancy effects are neglected in the present study, as only forced convection is considered. Consequently, all buoyancy-related terms are omitted from Eqs. (13) and (14). The model coefficients employed throughout Eqs. (13)–(21) are:

$$\begin{aligned}&\sigma_k = 1, \quad \sigma_\varepsilon = 1.3, \quad C_{\varepsilon 1} = 1.44, \quad C_{\varepsilon 2} = 1.92, \quad C_\mu = 0.09, \\ &C_{d_0} = 0.091, \quad C_{d_1} = 0.0042, \quad C_{d_2} = 0.00011, \quad C = 0.3, \quad D = 1, \\ &E = 0.00375, \quad C_l = 2.55, \quad C_w = 0.83\end{aligned} \tag{22}$$

The implemented formulation differs from Shams et al. (2014) in two main aspects. First, the sign in front of C and the exponential argument in Eq. (18) are modified so that f_ε is consistent with the formulation of Lien et al. (1996). Second, the Yap correction term S_Y is included following Shams (2018), with corrections to inconsistencies in the published equations. In particular, herein, the factor $1/\tau$ is retained in Eq. (14), the definition of S_Y is expressed in terms of ε/τ rather than ε^2/k, and the argument of the max operator in Eq. (21) is formulated using 0 instead of 1.

2.3. Thermal turbulence models

Thermal turbulence models provide a closure for the turbulent heat flux and govern the coupling between momentum and thermal transport. In contrast to momentum turbulence models, their formulation is directly influenced by the Prandtl number and often derived from approaches originally developed for $Pr \approx 1$. The models considered in this study can be grouped into three main categories: (i)

diffusivity-based approaches relying on a turbulent Prandtl number Pr_t, (ii) multi-equation models based on the transport of temperature variance and relative dissipation rate, and (iii) algebraic heat-flux models providing a direct closure for the turbulent heat flux.

The following subsections describe the specific formulations adopted in the present work, including the Kays correlation (KAYS), the multi-equation models MM (k_θ-ε_θ) and DAVIA (k_θ-Ω_θ), and the algebraic heat-flux model.

2.3.1. Turbulent Prandtl number model (KAYS)

The simplest approach to model the turbulent heat flux is based on a turbulent Prandtl number Pr_t, relating the turbulent thermal diffusivity to the turbulent viscosity through:

$$\alpha_t = \frac{\nu_t}{Pr_t}\,. \tag{23}$$

In this study, the correlation proposed by Kays (1994) is employed. This semi-empirical formulation provides a local expression for the turbulent Prandtl number as a function of the molecular Prandtl number and the turbulent viscosity ratio:

$$Pr_t = 0.85 + \frac{0.7}{Pr\,(\nu_t/\nu)} \tag{24}$$

The correlation above represents a purely local closure for the turbulent heat flux, since it depends explicitly on the local value of the turbulent viscosity ν_t. The turbulent heat flux is then obtained from the diffusivity-based closure defined as:

$$\overline{u_i' T'} = -\alpha_t \frac{\partial T}{\partial x_i} \tag{25}$$

The model therefore requires only the turbulent viscosity provided by the underlying momentum turbulence model. In the present work, this correlation is used in combination with the k–ω SST model as implemented in OpenFOAM v2212 (OpenCFD Ltd, 2022).

2.3.2. k_θ–ε_θ model (MM)

The MM model proposed by Manservisi and Menghini (2014a) is a combined turbulence model that employs the AKN formulation for momentum turbulence and a k_θ–ε_θ closure for thermal turbulence. It is a diffusivity-based model, where the turbulent heat flux is modeled with Eq. (25). The corresponding turbulent thermal diffusivity is given by:

$$\alpha_t = C_\theta k \tau_{l\theta} \tag{26}$$

where $\tau_{l\theta}$ is the local thermal characteristic time scale, which according to Manservisi and Menghini (2014a) is modeled as

$$\tau_{l\theta} = f_{1\theta}\tau_u Pr_{t\infty} + f_{2\theta}\tau_m + f_{3\theta}\tau_u \sqrt{\frac{2R}{Pr}}\,\frac{1.3}{\sqrt{Pr}R_t^{3/4}}\,, \tag{27}$$

in which the following time scales appear:

$$\tau_u = \frac{k}{\varepsilon}, \quad \tau_\theta = \frac{k_\theta}{\varepsilon_\theta}, \quad R = \frac{\tau_\theta}{\tau_u}, \quad \tau_m = \frac{2R\tau_u}{R + C_\gamma} \tag{28}$$

The weighting functions $f_{1\theta}$, $f_{2\theta}$ and $f_{3\theta}$ are defined as in Manservisi and Menghini (2015), with corrections and modifications with respect to the original formulation reported in Manservisi and Menghini (2014a):

$$f_{1\theta} = \left(1 - e^{-R_\delta\sqrt{Pr}/19}\right)\left(1 - e^{-R_\delta/14}\right)\,, \tag{29}$$

$$f_{2\theta} = f_{1\theta}\, e^{-(R_t/500)^2}\,, \tag{30}$$

$$f_{3\theta} = f_{1\theta}\, e^{-(R_t/200)^2} \tag{31}$$

The definitions of R_t and R_δ are given in Eq. (10). It should be noted that the expression of $f_{1\theta}$ differs from the one originally reported in Manservisi and Menghini (2014a, 2015), and follows the corrected form proposed in subsequent works (Da Vià et al., 2016; Da Vià and Manservisi, 2019). In particular, a minus sign is missing in the exponential argument of the second term in Eq. (29) in the original formulation.

The thermal turbulence quantities k_θ and ε_θ are obtained from the following transport equations:

$$\frac{\partial k_\theta}{\partial t} + u_i\frac{\partial k_\theta}{\partial x_i} = \frac{\partial}{\partial x_i}\left[\left(\alpha + \frac{\alpha_t}{\sigma_{k_\theta}}\right)\frac{\partial k_\theta}{\partial x_i}\right] + P_\theta - \varepsilon_\theta \tag{32}$$

$$\begin{aligned}\frac{\partial \varepsilon_\theta}{\partial t} + u_i\frac{\partial \varepsilon_\theta}{\partial x_i} = \frac{\partial}{\partial x_i}&\left[\left(\alpha + \frac{\alpha_t}{\sigma_{\varepsilon_\theta}}\right)\frac{\partial \varepsilon_\theta}{\partial x_i}\right] \\ &+ \frac{\varepsilon_\theta}{k_\theta}\left(C_{p1}P_\theta - C_{d1}\varepsilon_\theta\right) + \frac{\varepsilon_\theta}{k}\left(C_{p2}P_k - C_{d2}\varepsilon\right)\end{aligned} \tag{33}$$

The thermal production term appearing in Eq. (32) is defined as:

$$P_\theta = \alpha_t \frac{\partial T}{\partial x_i}\frac{\partial T}{\partial x_i}\,, \tag{34}$$

and the model coefficients are selected according to Manservisi and Menghini (2015):

$$\begin{aligned}&C_\theta = 0.1, \quad Pr_{t\infty} = 0.9, \quad C_\gamma = 0.3, \quad \sigma_{k_\theta} = 1.4,\\ &\sigma_{\varepsilon_\theta} = 1.4, \quad C_{p1} = 0.925, \quad C_{d1} = 1.0, \quad C_{p2} = 0.9\end{aligned} \tag{35}$$

In particular, the coefficient C_{d2} is defined as given in Manservisi and Menghini (2015):

$$C_{d2} = \left[1.9\left(1 - 0.3e^{-0.0237R_t^2}\right) - 1\right]\left(1 - e^{-0.1754R_\delta}\right)^2 \tag{36}$$

Different expressions for C_{d2} are reported in the literature. Specifically, Manservisi and Menghini (2014a) do not include the term -1 in the first bracket, while Manservisi and Menghini (2014b), Da Vià et al. (2016) adopt the same structure as Eq. (36) but with a different coefficient in the second exponential (0.0308 instead of 0.1754). In the present work, the latter value is adopted, consistently with the relation proposed by Abe et al. (1995), corresponding to 1/5.7.

More generally, the formulation of the MM model adopted here is based on a combination of expressions reported across different publications by the original authors. In several cases, discrepancies were identified, including inconsistent coefficients and missing terms. The final implemented formulation corresponds to a consistent set of equations obtained through cross-verification of the available sources and validation against reference results reported in the literature.

2.3.3. k_θ–Ω_θ model (DAVIA)

The DAVIA thermal turbulence model is used in combination with the KLW momentum model (Section 2.2.2) and is based on the formulation proposed by Da Vià et al. (2016), derived from the k_θ–ε_θ model of Manservisi and Menghini (2014a) (see Section 2.3.2). The model introduces Ω_θ as the second thermal turbulence variable, defined through the transformation $\varepsilon_\theta = C_\mu k_\theta e^{\Omega_\theta}$, once plugged into Eq. (33), yielding:

$$\begin{aligned}\frac{\partial \Omega_\theta}{\partial t} + u_i\frac{\partial \Omega_\theta}{\partial x_i} = \frac{\partial}{\partial x_i}&\left[\left(\alpha + \frac{\alpha_t}{\sigma_{\varepsilon_\theta}}\right)\frac{\partial \Omega_\theta}{\partial x_i}\right] + \frac{2}{k_\theta}\left(\alpha + \frac{\alpha_t}{\sigma_{\varepsilon_\theta}}\right)\frac{\partial k_\theta}{\partial x_i}\frac{\partial \Omega_\theta}{\partial x_i} \\ &+ \left(\alpha + \frac{\alpha_t}{\sigma_{\varepsilon_\theta}}\right)\frac{\partial \Omega_\theta}{\partial x_i}\frac{\partial \Omega_\theta}{\partial x_i} + \frac{C_{p1} - 1}{k_\theta}P_\theta + \frac{C_{p2}}{k}P_k + \\ &- C_\mu(C_{d1} - 1)e^{\Omega_\theta} - C_\mu C_{d2}e^{\Omega}\end{aligned} \tag{37}$$

The production terms P and P_θ are defined in Eqs. (3) and (34), respectively. The transport equation for k_θ remains identical to Eq. (32). Eq. (37) differs from the formulation reported by Da Vià et al. (2016) in the coefficient multiplying the term $(C_{d1} - 1)e^{\Omega_\theta}$, where the present implementation includes the factor C_μ, as required by the previously introduced transformation of ε_θ.

The thermal time scale $\tau_{l\theta}$ is computed using Eq. (27), consistently with the MM model. This differs from the formulation originally proposed by Da Vià et al. (2016), where only the first term is expressed as $f_{1\theta}\tau_u/Pr_{t\infty}$, i.e. dividing by $Pr_{t\infty}$ instead of multiplying by it, while the remaining terms are unchanged.

In addition, the value of $Pr_{t\infty}$ is taken equal to 0.9, as in the MM model, instead of the value $Pr_{t\infty} = 0.75188$ suggested by Da Vià and Manservisi (2019). The present implementation therefore differs from the original DAVIA formulation both in the first term of the time scale expression and in the value of $Pr_{t\infty}$.

The weighting functions $f_{1\theta}$, $f_{2\theta}$ and $f_{3\theta}$ are taken from Da Vià et al. (2016) and correspond to Eqs. (29) to (31). The coefficient C_{d2} is defined as in Eq. (36), following the discussion in Section 2.3.2. The model coefficients are selected according to Da Vià et al. (2016):

$$C_\mu = 0.09, \quad \sigma_{\varepsilon_\theta} = 1.4, \quad C_{p1} = 1.025, \quad C_{d1} = 1.1 \tag{38}$$

The coefficient C_{p2} is set to 0.9, consistently with the MM model, instead of the value 1.9 originally proposed by Da Vià et al. (2016).

As in the KLW model (Section 2.2.2), the cross-diffusion terms in Eq. (37) can be treated either explicitly or partially implicitly. Both options are available in the present implementation.

2.3.4. Algebraic heat-flux model (AHFM)

The algebraic heat-flux model considered in this study follows the formulation proposed by Shams et al. (2014), based on the model of Kenjeres et al. (2005). The adopted formulation corresponds to the so-called AHFM-NRG model, originally developed for low-Pr-number flows in forced, natural, and mixed convection regimes (Shams et al., 2014). An improved variant, referred to as AHFM-NRG+, was later introduced by De Santis and Shams (2018). The AHFM-NRG+ modifications concern the buoyancy-production contribution of the closure (coefficient C_{t3} in Eq. (39)), which vanishes identically for $g_i = 0$. Consequently, for the purely forced-convection cases considered here, AHFM-NRG and AHFM-NRG+ coincide, and the latter is not considered separately.

The AHFM provides a direct algebraic closure for the turbulent heat flux $\overline{T'u_i'}$, given by:

$$\overline{T'u_i'} = -C_{t0}\frac{k}{\varepsilon}\left(C_{t1}\overline{u_i'u_j'}\frac{\partial T}{\partial x_j} + C_{t2}\overline{T'u_j'}\frac{\partial u_i}{\partial x_j} + C_{t3}\beta g_i\, 2k_\theta\right) + C_{t4}\left(\frac{\overline{u_i'u_j'}}{k} - \frac{2}{3}\delta_{ij}\right)\overline{T'u_j'} \tag{39}$$

Consistently with the other models, buoyancy effects are neglected in all simulations ($g_i = 0$); the corresponding term is reported here only for completeness of the published formulation.

The Reynolds stresses $\overline{u_i'u_j'}$, k and ν_t are provided by the underlying momentum turbulence model, in this case ShamsKE (Section 2.2.3). The temperature variance k_θ is obtained from the following transport equation:

$$\frac{\partial(\rho k_\theta)}{\partial t} + u_i\frac{\partial(\rho k_\theta)}{\partial x_i} = \frac{\partial}{\partial x_i}\left[\rho\left(\alpha + \frac{\nu_t}{\sigma_{k_\theta}}\right)\frac{\partial k_\theta}{\partial x_i}\right] + \rho P_\theta - \rho\varepsilon_\theta\,, \tag{40}$$

where P_θ is defined in Eq. (34). In the AHFM-NRG formulation, the ratio of turbulent time scales R is assumed constant, leading to:

$$\varepsilon_\theta = \frac{k_\theta}{k}\frac{\varepsilon}{R} \tag{41}$$

with the constant time-scale ratio $R = 0.5$ Shams et al. (2014). The remaining model coefficients are $C_{t0} = 0.2$, $C_{t2} = 0.6$, $C_{t3} = 2.5$, $C_{t4} = 0.0$ and $\sigma_{k\theta} = 1.0$ Shams et al. (2014). It should be noted that Eq. (40) differs from Eq. (32) in the diffusion term, where ν_t is used instead of α_t.

When the AHFM is used in combination with the ShamsKE model, the coefficient C_{t1} is defined as (Shams et al., 2014):

$$C_{t1} = \begin{cases} 0.053\ln(Re\,Pr) - 0.27, & Re\,Pr > 180 \\ 0.25, & Re\,Pr \le 180 \end{cases} \tag{42}$$

A revised expression for C_{t1} was later proposed by Shams and De Santis (2019) for use with the EBRSM model, defined as

$$C_{t1} = 0.176\ln(Re\,Pr) - 0.426, \quad \text{for } Re\,Pr > 145$$

Since no specification is provided for $Re\,Pr \le 145$ in Shams and De Santis (2019), the value $C_{t1} = 0.25$ is assumed, in analogy with the original formulation of Shams et al. (2014) (Eq. (42)). The resulting implementation is therefore:

$$C_{t1} = \begin{cases} 0.176\ln(Re\,Pr) - 0.426, & Re\,Pr > 145 \\ 0.25, & Re\,Pr \le 145 \end{cases} \tag{43}$$

The present implementation allows switching between the two formulations of C_{t1}. In addition, the algebraic equation Eq. (39) can be solved either explicitly or implicitly. In the explicit approach, the turbulent heat flux appearing on the right-hand side is taken from the previous iteration, while in the implicit approach the linear system described by Eq. (39) is solved.

In the absence of buoyancy effects, i.e. when the gravitational term is neglected in Eq. (39), the turbulent heat flux becomes independent of k_θ. Therefore, for purely forced convection problems, the transport equation for k_θ does not need to be solved.

Finally, it should be noted that the coefficient C_{t1} depends on the Reynolds number Re, defined using global reference quantities. This introduces a non-local dependency, as these quantities are not uniquely defined in general flow configurations, except for canonical cases such as channel or pipe flows.

In the present work, Re is taken as the bulk Reynolds number of each configuration: $Re_b = 2\delta u_b/\nu$, based on the full channel height, for the channel; $Re_b = u_b D/\nu$ for the pipe; and the inlet bulk Reynolds number $Re_b = 2\,l_{\text{step}}u_b/\nu$ for the backward-facing step. For the channel ($Re_\tau = 395, 640$) and pipe configurations, where $Re\,Pr > 180$, the corresponding C_{t1} value follows directly from Eq. (42); for $Re_\tau = 180$, where $Re\,Pr \le 180$, the clamped value $C_{t1} = 0.25$ applies. For the backward-facing step, the value $C_{t1} = 0.0052$ is used, as detailed in Section 4.3.

Details on the implementation of the thermal turbulence models within the OpenFOAM framework, including the class structure and solver integration, are provided in Appendix.

3. Numerical setup and simulation details

This section describes the numerical setup adopted in the simulations. All cases presented in this study are provided as supplementary material to ensure full reproducibility and allow for independent verification and further analysis. In particular, all numerical settings, solver configurations, and case files can be retrieved on a case-by-case basis from the supplementary material, which contains the complete set of simulations performed in this work.

The working fluid is assumed to be Newtonian with constant thermophysical properties. The effects of gravity and viscous heating are neglected. The set of governing equations contains the steady-state continuity, momentum, and energy equations, Eqs. (44) to (46), which in Cartesian coordinates read as follows:

$$\frac{\partial u_i}{\partial x_i} = 0\,, \tag{44}$$

$$u_j\frac{\partial u_i}{\partial x_j} = -\frac{\partial(p/\rho)}{\partial x_i} + \nu\frac{\partial^2 u_i}{\partial x_j^2} - \frac{\partial}{\partial x_j}\left(\overline{u_i'u_j'}\right) + S_m\,, \tag{45}$$

$$u_i\frac{\partial\theta}{\partial x_i} = \alpha\frac{\partial^2\theta}{\partial x_i^2} - \frac{\partial}{\partial x_i}\left(\overline{u_i'\theta'}\right) + S_\theta \tag{46}$$

The Reynolds stress tensor $\overline{u_i'u_j'}$ is modeled according to Eq. (4), while the turbulent heat flux $\overline{u_i'\theta'}$ is modeled using Eq. (25) for diffusivity-based closures and Eq. (39) for the algebraic heat-flux model.

In the energy equation, θ represents the excess temperature for channel and pipe flows, defined as $\theta = \overline{T}_w - T$, being $\overline{T}_w$ the mean wall temperature. For the backward-facing step case θ is defined in Section 4.3.

For channel and pipe flow simulations, periodic boundary conditions are applied between the inlet and outlet to reproduce fully developed conditions. Additional source terms are thus added to the momentum and energy equations, in order to reproduce the effect of the linear change in pressure (due to friction, i.e. wall momentum flux) and temperature (as required by the chosen non-dimensionalization) along the streamwise direction in the periodic setting.

In Eq. (45), the source term S_m is implemented using the `meanVelocityForce` functionality available in OpenFOAM v2212 (`fvOptions`), enforcing a prescribed bulk velocity through a spatially uniform forcing term dynamically adjusted during the simulation.

In Eq. (46), the source term S_θ is implemented within a custom solver for the energy equation and takes different expressions for channel and pipe configurations:

$$S_\theta = \begin{cases} \dfrac{u_1 T^*}{\delta} & \text{channel flow} \\ \dfrac{4 u_1 T^*}{D} & \text{pipe flow} \end{cases}, \tag{47}$$

where u_1 denotes the streamwise velocity component and $T^* = q_w/(\rho c_p u_b)$, with q_w the imposed wall heat flux, ρ the density, c_p the specific heat at constant pressure, and u_b the bulk velocity.

The spatial discretization employs second-order accurate schemes for interpolation, as well as for the gradient, divergence, and Laplacian operators. The cross-diffusion terms arising in the KLW and DAVIA models (Sections 2.2.2 and 2.3.3) are treated explicitly.

A segregated solution strategy is adopted: the velocity and pressure fields are solved first, followed by the temperature field. This approach is justified by the assumption of constant fluid properties, under which the momentum equations are decoupled from the thermal field. Following OpenFOAM terminology, this strategy is referred to as a `frozen-flow` approach. The SIMPLE algorithm is used for the pressure-velocity coupling.

Under-relaxation factors are applied to all equations. Simulations are initialized with conservative values (typically 0.1), which are gradually increased to standard values during the iterative process to enhance convergence. Initial conditions are prescribed as uniform fields with values of the same order of magnitude as the expected solution.

Convergence to steady state is assumed when the normalized residuals of all momentum and thermal turbulence quantities fall below 10^{-9} in all reported cases.

3.1. Boundary conditions

Mixed boundary conditions are applied at the wall for the thermal turbulence variables, following Straub et al. (2019):

$$k_\theta|_w = 0\,, \tag{48}$$

$$\varepsilon_\theta|_w = \alpha \frac{2k_\theta}{d_w^2}\,, \tag{49}$$

$$\Omega_\theta|_w = \ln\left(\frac{2\alpha}{C_\mu d_w^2}\right), \tag{50}$$

$$\Omega|_w = \ln\left(\frac{2\nu}{C_\mu d_w^2}\right) \tag{51}$$

where d_w is the distance to the nearest wall, k_θ in Eq. (49) is evaluated at the cell center, $C_\mu = 0.09$ and the subscript w denotes the wall. The condition $k_\theta|_w = 0$ corresponds to an ideally isothermal wall. For the isoflux conditions considered here, temperature fluctuations at the wall do not vanish in general. However, all assessed closures were calibrated with $k_\theta|_w = 0$, and the reference data of Straub et al. (2019) show that, at the Prandtl numbers of interest, the influence of the thermal wall boundary condition on the mean temperature is small, while it mainly affects the near-wall temperature variance. This aspect must be kept in mind when comparing the $\sqrt{2k_\theta^+}$ profiles with the reference data.

Table 2
Boundary conditions at the wall (values reported without units).

Variable	Boundary condition
ε	$2\nu k_{cc}/d_w^2$
f	0
k	0
Ω	Eq. (51)
ω	$6\nu/(\beta_1 d_w^2)$
p	zero-gradient
R_{ij}	10^{-20}
u_i	0
ε_θ	Eq. (49)
k_θ	10^{-20}
Ω_θ	Eq. (50)
θ	0

The boundary conditions for further variables are summarized in Table 2. Here, k_{cc} denotes the turbulent kinetic energy at the center of the near-wall adjacent cell, and $\beta_1 = 0.075$ is the standard inner-blending coefficient of the k–ω SST model (Menter et al., 2003). The expressions for k, ε and ω correspond to those selectable through the respective low-Reynolds wall functions (`kLowReWallFunction`, `epsilonWallFunction`, `omegaWallFunction`) in OpenFOAM v2212 (OpenCFD Ltd, 2022). It should be noted that the elliptic relaxation factor f and the Reynolds stress components R_{ij} are required and thus solved only for the EBRSM model. The values 10^{-20} prescribed for k_θ and R_{ij} are numerically equivalent to zero and are used instead of an exact zero for solver stability.

4. Results and discussion

The following investigations assess the turbulence models in channel flow, pipe flow, and backward-facing step configurations with three objectives. First, to verify the reproducibility of results reported in the literature, given the discrepancies between the original model formulations and their implementation in the present work (see Section 2.1). Second, to evaluate the numerical robustness and convergence behavior of the models. Third, to assess their predictive accuracy against high-fidelity reference data for low-Prandtl-number flows ($Pr \ll 1$).

For the k-ω SST model, no additional verification of reproducibility is required, as the model is adopted without modification from OpenCFD Ltd (2022) and has been extensively validated in the literature.

4.1. Channel flow

A quasi-one-dimensional setup is adopted, with a single computational cell in both the streamwise and spanwise directions, and 200 cells in the wall-normal direction. A grid stretching is applied in the wall-normal direction with an expansion ratio of 10 from the wall towards the channel centerline. This ensures that the viscous sublayer is properly resolved in all simulations, with $y^+ < 1$, allowing for the use of a wall resolved approach (sometimes also called low-Reynolds-number in OpenFOAM). A constant wall heat flux is imposed at both walls. By varying the bulk velocity u_b, simulations are performed at friction Reynolds numbers $Re_\tau = u_\tau \delta/\nu = 180, 395, 640$, where $u_\tau = \sqrt{\tau_w/\rho}$ is the friction velocity and δ is the channel's half height. A Prandtl number of $Pr = 0.025$ is considered. The results are primarily presented for $Re_\tau = 395$, as similar trends are observed for the other Reynolds numbers.

The DNS data used for comparison with the RANS simulations originates from the DNS database provided by Kawamura (2004). The results presented in viscous units are scaled with u_τ, $T_\tau = q_w/(\rho c_p u_\tau)$ and ν.

As shown in Fig. 1(a), all turbulence models accurately reproduce the velocity profile u_1^+ in viscous units for $Re_\tau = 395$. Minor deviations

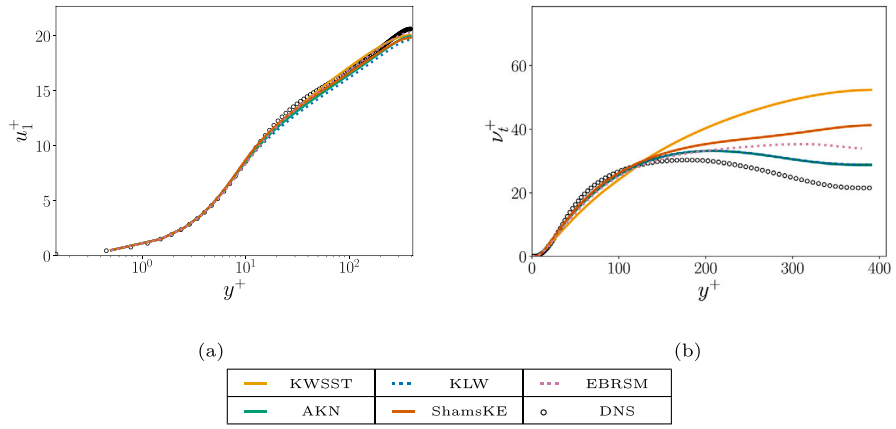


Fig. 1. (a) streamwise velocity $u_1^+ = u_1/u_\tau$ (b) Turbulent viscosity $\nu_t^+ = \nu_t/\nu$.
Source: DNS data from Kawamura (2004).

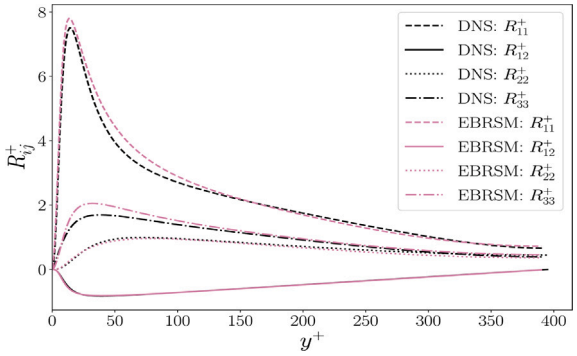


Fig. 2. Reynolds stresses in wall units ($R_{ij}^+ = \overline{u_i' u_j'}/u_\tau^2$) for EBRSM. DNS data from Kawamura (2004). Channel flow at $Re_\tau = 395$.

are observed for the KLW and ShamsKE models, both of which underestimate the velocity in the channel center compared to their respective reference studies.

The comparison of turbulent viscosity is shown in Fig. 1(b). The AKN and KLW models provide the best agreement with the DNS profile, with nearly identical curves. This should not surprise, since the KLW momentum turbulence model is derived from the AKN formulation. In contrast, for the EBRSM, which does not employ an eddy viscosity in its momentum closure, ν_t is evaluated a posteriori as the ratio of the turbulent shear stress to the mean strain rate, $\nu_{t,\text{eff}} = -\overline{u_1' u_2'}/(\partial u_1/\partial x_2)$, consistently with the evaluation of the DNS data. The resulting profile is in agreement with the DNS data in the near-wall region, while a moderate overestimation is observed towards the channel center, where both the turbulent shear stress and the mean velocity gradient vanish and their ratio becomes increasingly sensitive to small differences between the two quantities.

A complementary assessment of the EBRSM model is provided by the direct comparison of its Reynolds stress components with the DNS data, as shown in Fig. 2. The deviations between the EBRSM model results and the DNS data for the Reynolds stresses are minimal.

No significant numerical stability issues were observed for the KWSST-KAYS and AKN-MM combinations. Small variations in initial conditions did not lead to divergence, and convergent solutions could be obtained with equation relaxation factors above 0.7. The ShamsKE-AHFM model, when used without the Yap correction, also exhibited robust behavior with respect to the sensitivity to initial conditions. However, the Yap correction needed to be introduced gradually during the simulation. If the Yap correction was activated from the start with uniform initial conditions, no convergence could be achieved.

In contrast, the KLW-DAVIA and EBRSM-AHFM combinations required significantly smaller equation relaxation factors and were more sensitive to initial conditions. Increasing the initial values of Ω and R_{ij} by a factor of 10 resulted in solution divergence for both models. Thus, the improved numerical robustness claimed by Da Vià et al. (2016) for transitioning from the k-ε to the k-Ω model was not observed. This behavior is consistent with the logarithmic nature of $\Omega = \ln\omega$. In the robustness test reported here, the perturbation was applied directly to the logarithmic variable (Ω increased by a factor of 10), rather than to the physical dissipation rate ω. Since $\Omega = \ln\omega$, multiplying Ω by a factor of 10 corresponds to raising the physical variable to the tenth power, $\omega_{\text{new}} = (\omega_{\text{old}})^{10}$, rather than to a comparably moderate rescaling of ω itself. This is a substantially more severe perturbation than the initial-condition variations considered by Da Vià et al. (2016), and directly explains the divergence observed here through the exponential source terms e^{Ω} and e^{Ω_θ}, without contradicting the robustness reported therein for physically-scaled initial fields.

In principle, the solution of the momentum equation, represented in nondimensional form, should depend only on the Reynolds number and not on the specific values of the dimensional quantities used to define it. However, for the EBRSM model, a different behavior was observed. When using a low kinematic viscosity (of order $10^{-7}\,\text{m}^2/\text{s}$), no converged turbulent solution could be obtained, and the simulations invariably relaminarized, even at $Re_\tau = 395$. In contrast, using a higher viscosity (of order $10^{-3}\,\text{m}^2/\text{s}$) at the same Reynolds number led to a converged turbulent solution. Since the model equations are dimensionally consistent and the non-dimensional solution depends on the Reynolds number only, this behavior must be attributed to the numerical treatment rather than to the model formulation. Possible mechanisms include absolute solver tolerances and dimensional clipping and limiting operations in the implementation, whose effect does not scale with the magnitude of the flow variables.

The results for the temperature θ, turbulent thermal diffusivity α_t, and turbulent heat flux component normal to the wall $\overline{u_2'\theta'}$ in wall units are shown in Fig. 3. For the two AHFM-based combinations (ShamsKE-AHFM and EBRSM-AHFM), which do not rely on the gradient-diffusion hypothesis, the thermal diffusivity is computed a posteriori as $\alpha_t = -\overline{u_2'\theta'}/(\partial\theta/\partial x_2)$, where the subscript 2 denotes the wall-normal direction.

The KWSST-KAYS combination closely reproduces the DNS temperature profile, although it underestimates the wall-normal turbulent heat flux (Fig. 3(c)). At $Pr = 0.025$, molecular conduction ($\alpha^+ = 1/Pr = 40$) remains the dominant transport mechanism over most of the channel, so that the mean temperature is only weakly sensitive to inaccuracies in α_t. The accurate temperature prediction must therefore be attributed primarily to the very low Prandtl number.

Note that, at the low Prandtl number considered here, bulk metrics such as the Nusselt number are only weakly sensitive to inaccuracies in the modeled turbulent heat flux, as molecular conduction dominates the energy balance. The profile-resolved comparisons of temperature and turbulent heat flux presented here are therefore more diagnostic of the underlying closure behavior than an integrated heat-transfer coefficient would be. This does not apply to the local Nusselt number reported for the backward-facing step (Section 4.3, Fig. 8(c)), where convective transport in the recirculation and reattachment regions, rather than molecular conduction, controls the local heat transfer.

The AKN-MM, KLW-DAVIA, and EBRSM-AHFM combinations successfully reproduce the results reported by their respective authors in the literature. However, the ShamsKE-AHFM model does not match the results presented by Shams et al. (2014) and shows significant deviations from DNS data at $Re_\tau = 395$, with similar behavior also observed at other Reynolds numbers. Due to this inconsistency, the ShamsKE-AHFM combination is excluded from the accuracy assessment. Its results are nevertheless reported for the pipe and backward-facing step configurations in order to verify whether the lack of reproducibility is systematic and thereby to isolate its origin. It should be noted that different implementations of the ShamsKE-AHFM model exist across CFD platforms. In particular, Shams et al. (2014) performed their simulations using STAR-CCM+ (Siemens Digital Industries Software, 2012), while Shams and De Santis (2019) employed CODE SATURNE (Archambeau et al., 2004), whereas the present work is based on OpenFOAM v2212. Due to the limited level of detail provided in the original publications, these implementations may differ in terms of model coefficients, auxiliary functions, and numerical treatment. This lack of a uniquely defined and fully documented formulation can lead to significant discrepancies between reported results and independent implementations. The deviations observed in the present work, particularly for the ShamsKE model, are therefore likely not only related to numerical aspects, but also to differences in the underlying model formulation.

Since the results obtained with the ShamsKE momentum model are able to reproduce those reported by Shams et al. (2014), it can be inferred that the observed discrepancies are likely associated with the implementation or modeling of the explicit expression for the turbulent heat flux, rather than with the underlying momentum turbulence model. The fact that the EBRSM-AHFM combination is able to reproduce the results reported by Shams and De Santis (2019), obtained with a different CFD code, does not allow isolating the exact origin of the discrepancies observed for the ShamsKE-AHFM combination.

The numerical robustness issues observed for the EBRSM and KLW models in the channel flow configuration could, in principle, justify their exclusion from further analysis. However, with appropriate numerical settings, both models are able to reproduce the results reported by their respective authors and show good agreement with DNS data. For this reason, they are retained and further evaluated in turbulent pipe flow simulations, as discussed in Section 4.2.

4.2. Pipe flow

The turbulent pipe flow configuration is considered as a second canonical test case to further assess the reproducibility of the different turbulence models beyond the channel flow. A fully developed flow is simulated using periodic boundary conditions in the streamwise direction. A constant and spatially uniform wall heat flux is imposed along the pipe wall. The simulations are performed on a so-called *O-ring mesh*, shown in Fig. 4, to avoid singularities at the pipe centerline, while ensuring sufficient near-wall resolution to capture the viscous sublayer. A single cell is used in the streamwise direction, while 4992 cells are employed in the pipe cross-section.

The same modeling assumptions as in the channel flow are retained, including constant fluid properties, neglect of buoyancy effects, and the use of a segregated solution strategy in which the flow field is solved prior to the thermal field (`frozen-flow` approach). Compared to the channel flow, the pipe configuration introduces an increased geometrical complexity due to the non Cartesian, not exactly orthogonal mesh, allowing for a more stringent assessment of numerical robustness.

The data used for comparison with the RANS simulations originate from the database provided by Straub (2023). No pipe flow simulations were presented for the EBRSM-AHFM combination in Shams and De Santis (2019). The simulations are performed at a bulk Reynolds number $Re_b = u_b D/\nu = 11\,700$ and a Prandtl number $Pr = 0.025$, matching the conditions of the reference database, where u_b is the imposed bulk velocity and D is the pipe diameter.

Fig. 5 presents the high-resolution LES data from Straub (2023) alongside the RANS simulation results for selected variables in wall units. The results show qualitative similarities to those observed in channel flow at $Re_\tau = 395$, thus only the key differences between the models will be discussed rather than a detailed profile-by-profile comparison.

The reproducibility of the implemented models is first assessed by comparison with results available in the literature. For the AKN-MM and KLW-DAVIA combinations, Manservisi and Menghini (2014a), Da Vià et al. (2016) report profiles of θ^+ at $Re_\tau = 395$ and $Pr = 0.025$, although only in logarithmic representation, which limits a direct quantitative comparison. However, Manservisi and Menghini (2014a) provide temperature standard deviation profiles with linear scaling, enabling a more meaningful assessment.

For the present pipe flow configuration at $Re_b = 11700$, the MM and DAVIA models yield an estimated $Re_\tau \approx 370$. At this value, the AKN-MM combination slightly overestimates $\sqrt{2k_\theta^+}$ compared to the results reported by Manservisi and Menghini (2014a) at $Re_\tau = 395$. A similar trend was already observed in the channel flow case, indicating a systematic behavior of the model. Despite these differences, the overall profile is well captured. For the DAVIA model, no reference data for $\sqrt{2k_\theta^+}$ in cylindrical geometries are available in Da Vià et al. (2016), preventing a direct comparison.

Following this verification, the models are compared against the reference data of Straub (2023). As shown in Fig. 5, all models accurately reproduce the mean velocity profile. The turbulent heat flux is also well captured by all models, with the exception of KWSST-KAYS, which slightly underestimates it outside the core region. As discussed in Section 4.1, at $Pr = 0.025$ this has only a minor effect on the mean temperature due to the dominance of molecular conduction. Consequently, all models predict the mean temperature profile with minor deviations, primarily in the core flow region.

As discussed in Section 4.1, at this Prandtl number bulk metrics such as the Nusselt number are only weakly diagnostic of the accuracy of the modeled turbulent heat flux; for this reason, no Nusselt-number comparison is reported for the pipe flow, and the profile-resolved comparisons above are retained as the primary basis for assessing model accuracy.

Regarding temperature fluctuations, the AKN-MM and KLW-DAVIA combinations reproduce the overall behavior of the LES data, although a slight overestimation of the temperature standard deviation is observed, consistent with the channel flow results. The EBRSM-AHFM model exhibits a more pronounced overestimation, in line with the trends already identified in the channel configuration.

In terms of numerical robustness, no significant differences are observed compared to the channel flow simulations. The convergence behavior and sensitivity to initial conditions remain consistent across both geometries.

In both channel and pipe flows, only one component of the Reynolds stress tensor and turbulent heat flux directly affects the first-order moments. As a result, these configurations provide limited insight into the full behavior of the models. To enable a more comprehensive assessment, a flow case with multi-directional gradients and coupled interactions is required. For this purpose, the models are next evaluated in a two-dimensional backward-facing step configuration in the following section.

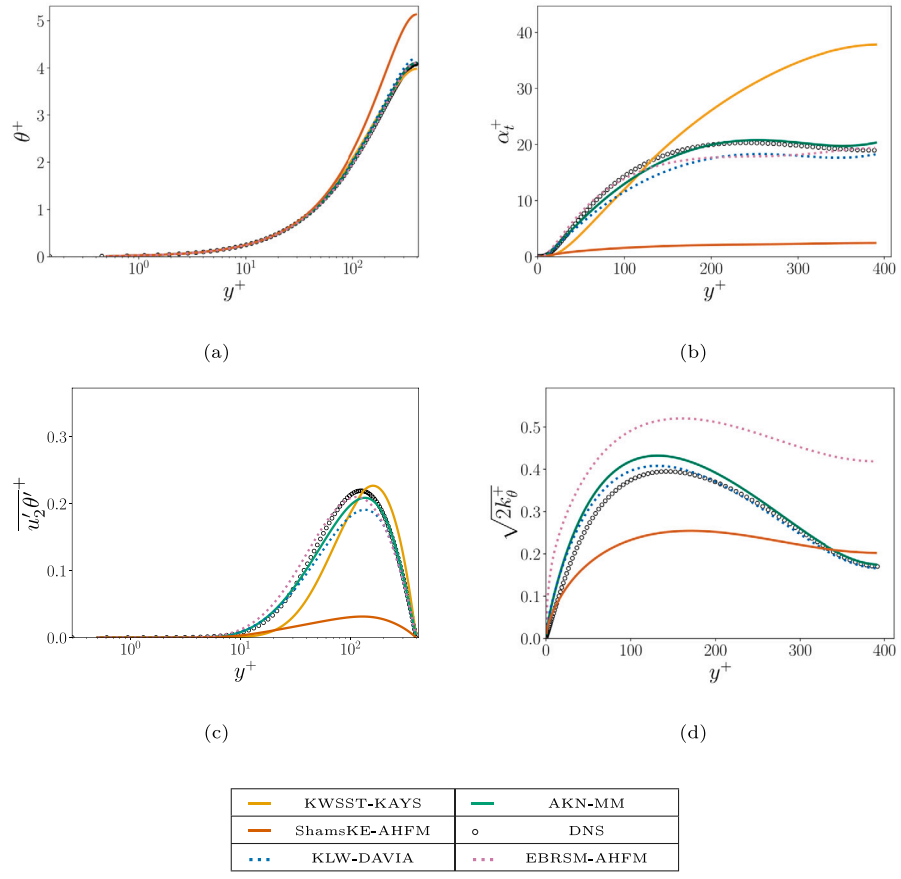


Fig. 3. (a) normalized temperature $\theta^+ = \theta/T_\tau$, (b) turbulent thermal diffusivity ($\alpha_t^+ = \alpha_t/\alpha$), (c) wall-normal turbulent heat flux $\overline{u_2'\theta'}^+ = \overline{u_2'\theta'}/(u_\tau T_\tau)$ (d) temperature standard deviation $\sqrt{2k_\theta^+} = \sqrt{2k_\theta}/T_\tau$.
Source: DNS data from Kawamura (2004).

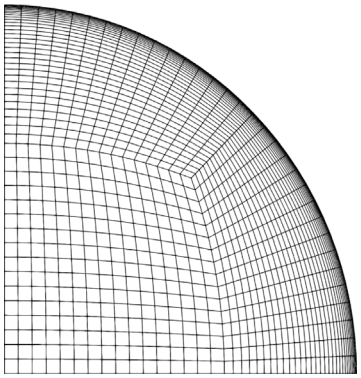


Fig. 4. One-fourth of the mesh in the pipe cross section.

4.3. Backward Facing Step (BFS)

The backward-facing step (BFS) configuration is considered to assess the performance of the turbulence models in a more complex flow geometry compared to channel and pipe flows. In addition, the simulations are performed at a lower Prandtl number ($Pr = 0.0088$), selected to match the available DNS reference data of Niemann and Fröhlich (2016).

Available reference results for this configuration are limited. Schumm et al. (2015) examined the AKN-MM combination and KWSST-KAYS, while De Santis and Shams (2018) considered the ShamsKE-AHFM combination. No reference data are available for the DAVIA and EBRSM-AHFM combinations. Despite the discrepancies observed in channel flow, the ShamsKE-AHFM combination is included in order to verify whether the lack of reproducibility is systematic, consistently with the rationale discussed in Section 4.1.

The BFS geometry is illustrated in Fig. 6. The streamwise dimensions of the domain are defined relative to the step height l_{step}, with $l_{\text{in}}/l_{\text{step}} = 2$, $l_{\text{out}}/l_{\text{step}} = 10$, and $l_{\text{top}}/l_{\text{step}} = 22$. The expansion ratio is $ER = L_{\text{step}}/(L_{\text{step}} - l_{\text{step}}) = 1.5$. The setup follows that of De Santis and Shams (2018), featuring an adiabatic section absent in Niemann and Fröhlich (2016). The computational mesh consists of 128,800 cells, refined to ensure $y^+ < 1$ across all cases.

Following Niemann and Fröhlich (2016), the inlet bulk Reynolds number is set to $Re_b = 2 l_{\text{step}} u_b/\nu = 9610$. Velocity and momentum turbulence variables are initialized using profiles obtained from fully developed channel flow simulations, as exemplified by the inlet profile $u_{1,\text{ch}}$ shown in Fig. 6. The pressure at the inlet has a zero-gradient condition, while the temperature is fixed at T_{ref}. According to Schumm et al. (2015), small initial values are prescribed for k_θ and ϵ_θ, with Ω_θ computed accordingly.

At the outlet, a Dirichlet condition of zero pressure is applied, while other variables follow zero-gradient conditions. A portion of the downstream wall is heated, while other sections remain adiabatic. A constant and uniform heat flux q_w is applied at the heated section.

For the EBRSM-AHFM model, $C_{t1} = 0.0052$ is used following De Santis and Shams (2018), instead of the value $C_{t1} = 0.25$ obtained from Eq. (42) or Eq. (43). This choice stems from the formulation adopted by De Santis and Shams (2018), where, for $Re\,Pr < 180$, the value $Re\,Pr = 180$ is used in Eq. (42), leading to a reduced value of C_{t1}.

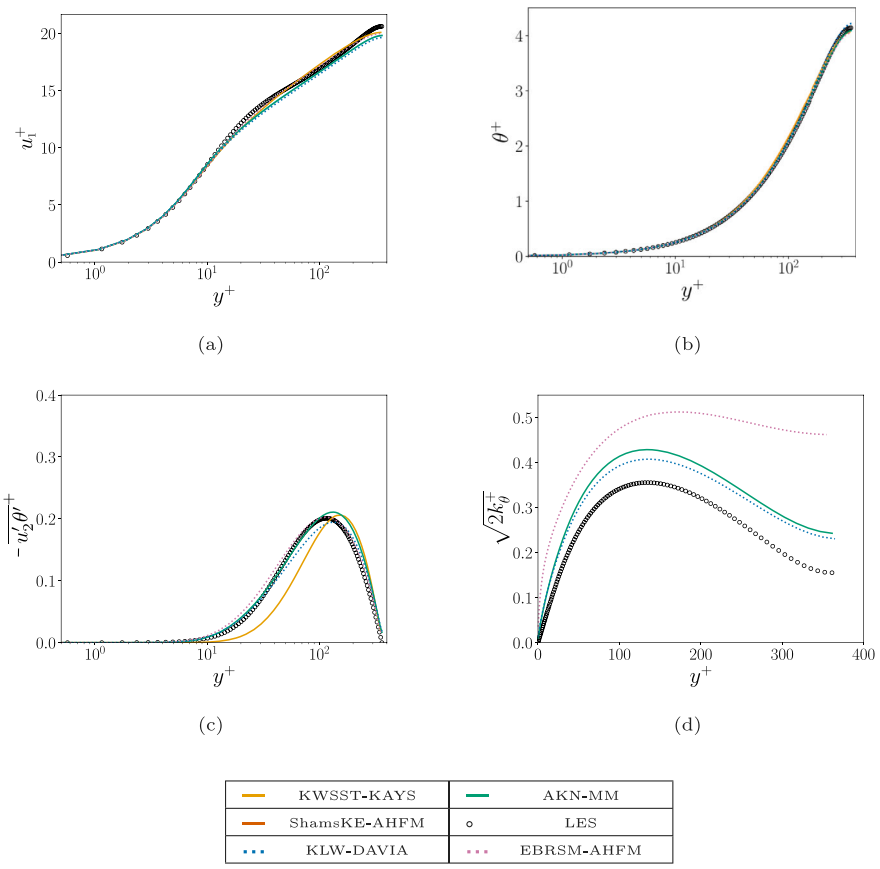


Fig. 5. (a) streamwise velocity $u_1^+ = u_1/u_\tau$ (b) temperature $\theta^+ = \theta/T_\tau$, (c) wall-normal turbulent heat flux $-\overline{u_2'\theta'}^+ = -\overline{u_2'\theta'}/(u_\tau T_\tau)$ (d) temperature standard deviation $\sqrt{2k_\theta}^+ = \sqrt{2k_\theta}/T_\tau$.
Source: LES data from Straub (2023).

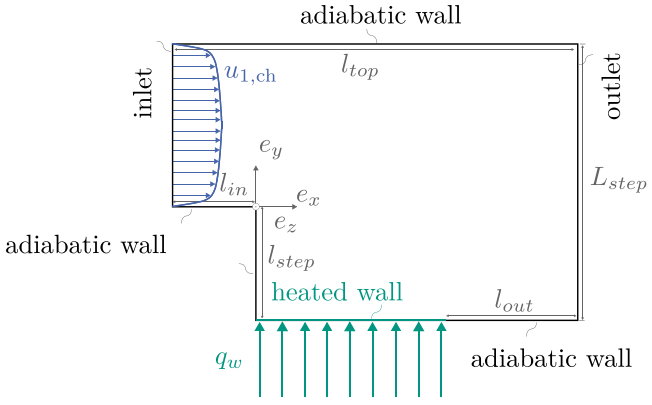


Fig. 6. Schematic (not to scale) of the backward-facing step configuration. $u_{1,\mathrm{ch}}$ represents the prescribed inlet velocity profile obtained from a fully developed turbulent channel flow.

Steady-state simulations are performed with constant fluid properties. Central-difference schemes are applied to the diffusive terms, while linear upwind schemes are used for the advective terms. The energy equation is solved using a *frozen-flow* approach after convergence of the velocity field. For the thermal turbulence models MM, DAVIA, and AHFM, the initial temperature field is obtained from simulations with a constant turbulent Prandtl number equal to 1. Convergence is assumed when the residuals of the thermal variables drop below 10^{-6}.

For the EBRSM model, no converged turbulent solution could be obtained for any of the tested numerical settings, despite using different orders of magnitude of ν, various initial conditions, numerical schemes, and equation under-relaxation factors. Consequently, no results are presented for the EBRSM-AHFM combination.

It should be noted that converged EBRSM solutions for BFS and separated flows have been reported in the literature with other codes, notably with the reference implementation in Code_Saturne (Manceau, 2015; Shams and De Santis, 2019). This supports the interpretation that the convergence issues observed here are related to the numerical treatment of the present OpenFOAM implementation rather than to the model formulation itself. A comparison with the alternative OpenFOAM implementation recently released by Gajetti et al. (2024) is envisaged to isolate the origin of these issues.

A converged turbulent solution for the momentum-related variables could be obtained using the KLW model. However, all simulations involving the thermal turbulence model KLW-DAVIA diverged. This behavior may be attributed to the cross-diffusion terms appearing in the transport equations of the thermal turbulence variables, as described in Section 2.3.3. For sufficiently large gradients, these terms can become dominant compared to the other contributions in the transport equations, potentially leading to divergence. Since no converged solution could be achieved for the thermal turbulence model, only the results of the KLW momentum model are presented.

The results of the turbulence models are presented in terms of the mean velocity in the streamwise and wall-normal directions in Figs. 7(a) and 7(b) at different downstream locations, up to a distance of $2/3\,L_{\mathrm{step}}$ from the lower wall. The skin friction coefficient c_f along the heated wall is shown in Fig. 7(c). Following Schumm et al. (2015), it is defined as $c_f = \tau_w/(0.5\rho u_{b,\mathrm{in}}^2)$, being τ_w the wall-shear stress and $u_{b,\mathrm{in}}$ the inlet bulk velocity.

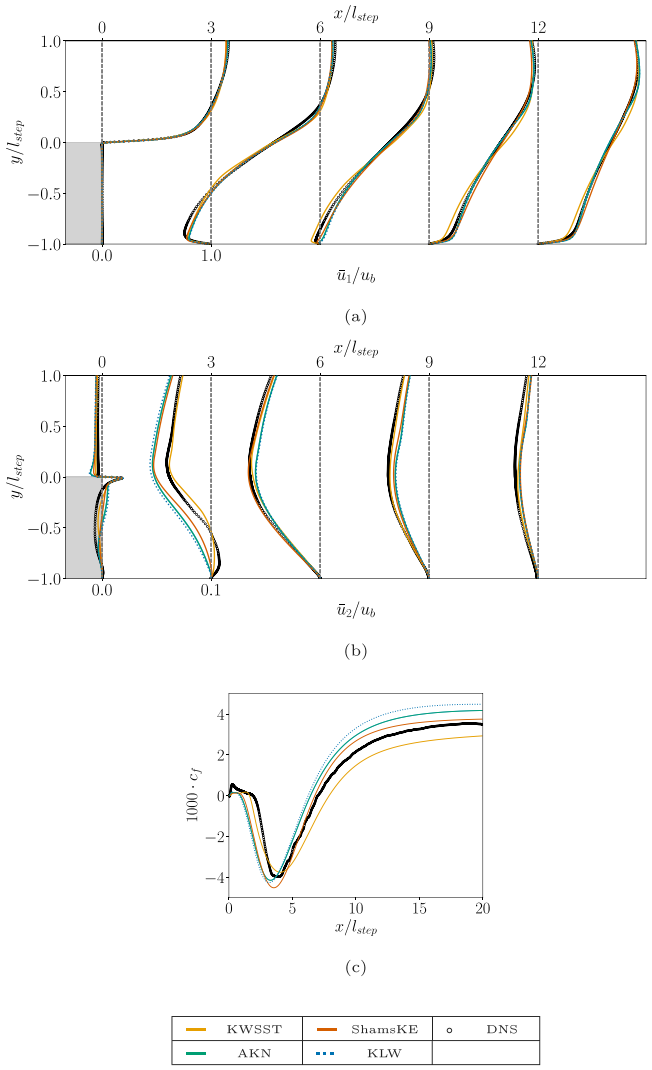


Fig. 7. (a) streamwise velocity, (b) wall-normal velocity, (c) skin friction coefficient c_f along the heated wall section.
Source: DNS data from Niemann and Fröhlich (2016).

The solutions for the momentum-related quantities obtained with the KWSST and AKN models are consistent with the results reported by Schumm et al. (2015). Similarly, the ShamsKE model reproduces the results of De Santis and Shams (2018). This provides further evidence that the implemented variant is consistent with that used by Shams et al. (2014), suggesting that the discrepancies observed for the ShamsKE-AHFM combination in channel flow are likely related to the thermal turbulence model.

Since the KLW model is derived from the AKN model, their results show very similar trends, as illustrated in Figs. 7(a) and 7(b). Owing to this similarity, the discussion focuses primarily on the AKN model. Given the good agreement with the results reported by the original authors, only selected aspects are discussed in the following.

As shown in Figs. 7(a) and 7(b), the KWSST model provides the best agreement with the DNS mean velocity upstream of the reattachment point, located at $x/l_{\text{step}} = 7.01$ according to Niemann and Fröhlich (2016). The skin friction coefficient, shown in Fig. 7(c), is also well captured upstream of the reattachment point. Downstream thereof, c_f increases gradually, reflecting the development of the boundary layer, in agreement with Schumm et al. (2015). Overall, the KWSST model accurately predicts the recirculation region.

According to De Santis and Shams (2018), the corresponding ShamsKE model exhibits the largest deviation from DNS in terms of c_f in the region close to the step. In addition, the size of the corner vortex is underestimated, a behavior that is also observed for the AKN model. Both the AKN and ShamsKE models overpredict the velocity in the wall-normal direction at $x/l_{\text{step}} = 3$.

Downstream of the reattachment point, the ShamsKE model provides the best agreement with the DNS skin friction coefficient among all considered models. It also predicts the reattachment location with the smallest deviation.

An accurate prediction of heat transfer requires a reliable representation of the flow field. All momentum turbulence models capture the main features of the mean velocity field at least qualitatively. However, the AKN, KLW, and ShamsKE models show noticeable deviations in the prediction of the recirculation region, while the KWSST model exhibits larger discrepancies in the downstream velocity field beyond the reattachment point.

The results for selected thermal quantities are presented in Fig. 8. Following Niemann and Fröhlich (2016), the excess temperature $\theta = (T - T_{\text{ref}})/\Delta T$ is used, with $\Delta T = q_w l_{\text{step}}/\lambda$, being λ the fluid's thermal conductivity. The distribution of the excess temperature is shown in Fig. 8(a), while profiles of the wall-normal turbulent heat flux at different downstream locations are reported in Fig. 8(b), up to a distance of $2/3\, L_{\text{step}}$ from the lower wall.

The AKN-MM combination reproduces the results reported by Schumm et al. (2015), and reference is therefore made to their discussion for a more detailed interpretation. Consistent with the channel flow case, the ShamsKE-AHFM combination fails to reproduce the temperature-related results reported by De Santis and Shams (2018). Since the momentum part of this combination (ShamsKE) does reproduce the reference velocity and skin-friction results discussed above, this confirms that the lack of reproducibility originates specifically from the thermal closure, and is systematic across flow configurations rather than case-dependent. For this reason, the corresponding temperature-related results are not discussed further in the following.

As shown in Fig. 8(b), the wall-normal turbulent heat flux is generally underestimated by the AKN-MM and KWSST-KAYS combinations, particularly downstream of the reattachment point. This leads to corresponding deviations in the predicted temperature field, especially in the near-wall region.

While, in channel flow, discrepancies in the temperature field can be largely attributed to inaccuracies in the wall-normal turbulent heat flux, this simplification does not hold for the BFS case. Here, the temperature field is influenced not only by $\overline{u_2'\theta'}$, but also by the accuracy of the predicted velocity field, due to the two-dimensional nature of the flow and the presence of strong spatial gradients.

Furthermore, the dependence of the thermal turbulence models on the underlying momentum model complicates the interpretation of the results. In particular, since the MM model is combined with the AKN momentum model, part of the observed differences can be attributed to the interaction between the thermal and momentum closures rather than to the thermal model alone.

For a clearer representation of the wall temperature, the local Nusselt number Nu_x along the heated wall is shown in Fig. 8(c). Following Schumm et al. (2015), it is defined as

$$Nu_x = \frac{q_w\, l_{\text{step}}}{\lambda\left(T_w - T_{\text{ref}}\right)} = \frac{1}{\theta_w} \tag{52}$$

Thus, Nu_x is inversely proportional to the excess temperature at the wall. For the DNS data, the maximum wall temperature occurs within the recirculation region, a behavior that is also captured by all models.

In the region close to the step, the KWSST-KAYS combination provides the best agreement with the DNS Nu_x distribution. However, downstream, it overpredicts the wall temperature. This can be attributed to the overestimation of the recirculation length, which delays the recovery of the boundary layer and reduces the wall temperature due to enhanced mixing with colder fluid. The AKN-MM combination overestimates Nu_x within the recirculation region but provides the best agreement in the downstream region compared to the other models.

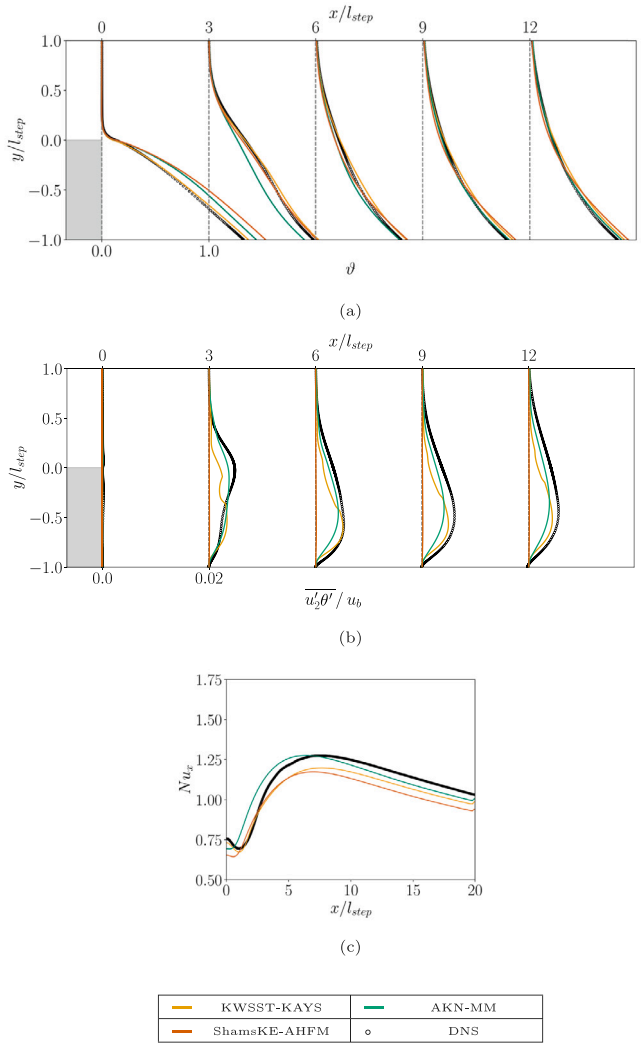


Fig. 8. (a) excess temperature, (b) wall-normal turbulent heat flux, (c) local Nusselt number Nu_x along the heated wall section.
Source: DNS data from Niemann and Fröhlich (2016).

5. Summary and conclusions

This study assessed turbulence models for simulating low-Prandtl-number flows in channel, pipe, and backward-facing step configurations. The models were evaluated in terms of reproducibility of reference results, numerical robustness, and predictive accuracy against DNS and high-fidelity data. A key outcome of this study is that several models cannot be reliably assessed for low-Prandtl-number flows due to limitations in reproducibility and numerical stability.

The KWSST-KAYS combination consistently provided accurate predictions of the mean temperature field across all cases, although the underlying turbulent heat flux is systematically underestimated (Sections 4.1 to 4.3). This accuracy must therefore be attributed primarily to the very low Prandtl number of the flows considered, rather than to an accurate representation of the turbulent heat transport. In the BFS configuration, a slight underestimation of the local Nusselt number was observed downstream of reattachment, likely related to limitations of the underlying turbulence closure. Despite this, the k–ω SST model accurately captured the mean velocity field in the recirculation region, highlighting the robustness of this approach. The simplicity and local nature of the Kays correlation further contribute to its computational efficiency and robustness.

Table 3
Overview of model reproducibility, robustness, and recommendation for low-Prandtl-number flow simulations based on results from channel, pipe, and BFS cases.

Model	Reproducibility	Robustness	Recommendation
KWSST-KAYS	Good	Good	Recommended
AKN-MM	Good	Good	Recommended
KLW-DAVIA	Good	Limited	Not recommended
ShamsKE-AHFM	Limited	Good	Not recommended
EBRSM-AHFM	Good	Limited	Further investigation

The AKN-MM combination demonstrated strong reproducibility, matching reference results from the literature for channel, pipe, and BFS cases. While minor discrepancies were observed in temperature variance, the model provided consistent and accurate predictions of temperature and Nusselt number distributions, making it a reliable option for low-Prandtl-number flow simulations.

The KLW-DAVIA combination reproduced trends similar to AKN-MM but exhibited significantly reduced numerical robustness. Small variations in the initial conditions of Ω led to divergence in channel flow, contradicting the improved robustness claimed by Da Vià et al. (2016). In the BFS configuration, the thermal model failed to converge entirely. This instability is likely associated with nonlinear source terms involving e^{Ω} and e^{Ω_θ}. As discussed in Section 4.1, this follows from the perturbation being applied to the logarithmic variable Ω itself (rather than to ω), which corresponds to raising the physical dissipation rate to the tenth power and strongly amplifies the exponential source terms e^{Ω} and e^{Ω_θ}. Given the similar predictive behavior but inferior robustness, the KLW-DAVIA combination does not provide advantages over AKN-MM.

The ShamsKE-AHFM combination showed inconsistent performance. While the ShamsKE momentum model reproduced reference results, the coupled thermal model failed to match published data and exhibited significant deviations in Nusselt number predictions. These discrepancies are likely due to differences in model implementation across CFD platforms and to the lack of a uniquely defined formulation in the literature.

The EBRSM-AHFM combination reproduced reference results in channel flow but showed limited numerical robustness: converged solutions were highly sensitive to the absolute value of the kinematic viscosity and to the initial Reynolds stress conditions, a behavior attributed to the numerical treatment rather than to the model formulation (Section 4.1). In the BFS configuration, no converged solution could be obtained, indicating limited applicability of this approach. One possible source of the discrepancies observed for the EBRSM-AHFM combination is the use of different EBRSM implementations. In the present work, the OpenFOAM implementation based on Manceau (2015) is adopted, whereas Shams and De Santis (2019) refer to a version based on Lardeau and Manceau (2014). A future comparison using the same EBRSM implementation, which is now available for OpenFOAM from Gajetti et al. (2024), would help isolate the origin of these differences in channel and pipe flow, and verify whether the same implementation resolves the convergence issues observed in the backward-facing-step configuration.

A fundamental limitation of the AHFM formulation is its dependence on the Reynolds-number-based coefficient C_{t1}, which introduces an inherent non-local dependency. The definition of the Reynolds number relies on global reference quantities, which are not uniquely defined in complex geometries, thereby limiting the general applicability of the model.

Overall, only a limited subset of models can be considered reliable for low-Prandtl-number flows, as many approaches are affected by either insufficient robustness or lack of reproducibility. The KWSST-KAYS and AKN-MM combinations emerge as the most consistent and reliable choices within the present assessment.

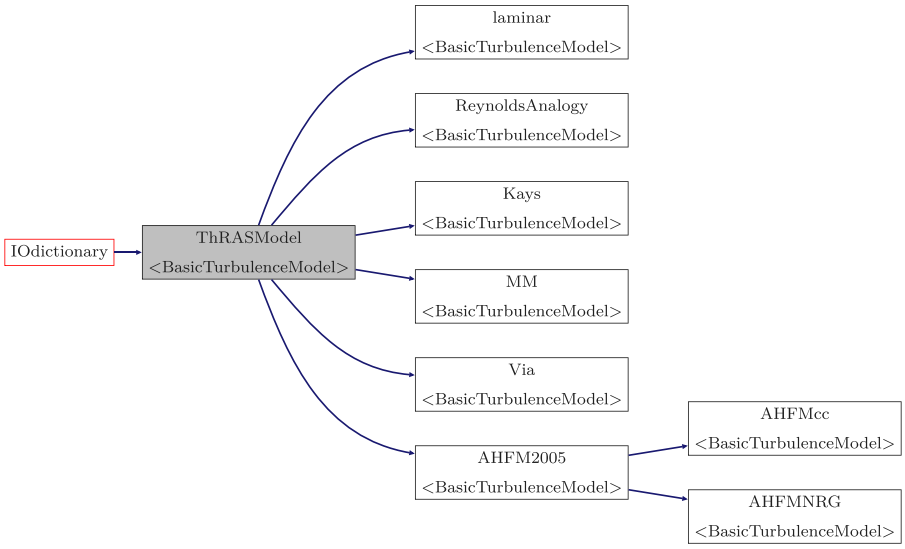


Fig. A.9. Class hierarchy of the `ThRASModel` framework for thermal turbulence models in OpenFOAM. The names appearing in the diagram are the implementation names used in the code and may differ from the model abbreviations adopted in the paper, such as `Via` for DAVIA and `AHFMNRG` for AHFM.

A summary of model performance in terms of reproducibility, robustness, and recommended usage is provided in Table 3. The present study highlights the importance of consistent model formulation and implementation when assessing turbulence closures for low-Prandtl-number heat transfer. The present findings apply to the investigated Prandtl-number range $0.0088 \leq Pr \leq 0.025$. No claim is made regarding model performance at higher Prandtl numbers.

CRediT authorship contribution statement

L. Marocco: Writing – original draft, Supervision, Conceptualization. **J. Schmitt:** Validation, Software, Investigation. **J. Neuhauser:** Writing – review & editing, Supervision. **B. Frohnapfel:** Writing – review & editing, Supervision, Project administration, Funding acquisition. **D. Gatti:** Writing – original draft, Supervision.

Declaration of generative AI and AI-assisted technologies in the manuscript preparation process

During the preparation of this work, the author L. Marocco used ChatGPT (OpenAI) for spell-checking and for grammar and style improvements. After using this tool, the author reviewed and edited the content as needed. All authors reviewed the final manuscript and take full responsibility for the content of the published article.

Declaration of competing interest

The authors declare that they have no known competing financial interests or personal relationships that could have appeared to influence the work reported in this paper.

Acknowledgments

Support by the German Research Foundation (DFG) under research project 423710075 is greatly acknowledged.

Appendix. Implementation of thermal turbulence models in OpenFOAM

The thermal turbulence models have been implemented within OpenFOAM v2212 using the abstract base class `ThRASModel`, which provides a unified interface for all thermal closures. The use of the template parameter `BasicTurbulenceModel` ensures compatibility with both incompressible and compressible momentum turbulence models.

All thermal models are derived from this base class and are selected at run-time through the standard OpenFOAM run-time selection mechanism. This design enables a modular coupling between momentum and thermal turbulence models, allowing different combinations to be systematically tested within a consistent numerical framework.

In addition to the models considered in the present study, further implementations such as `laminar`, `AHFM2005`, and `AHFMcc` are available but are not investigated here. The `laminar` model corresponds to $\alpha_t = 0$. The implemented models are integrated into the steady-state solvers `simpleFoamThRAS` and `chtMultiRegionSimpleFoamThRASSolid`. The former extends the standard `simpleFoam` solver by including the energy equation and thermal turbulence closures, while the latter enables simulations with separate fluid and solid regions, allowing for the treatment of conjugate heat transfer problems.

A schematic representation of the class hierarchy is shown in Fig. A.9.

Data availability

The data will be made available upon final acceptance.

References

Abe, K., Kondoh, T., Nagano, Y., 1994. A new turbulence model for predicting fluid flow and heat transfer in separating and reattaching flows - I. Flow field calculations. Int. J. Heat Mass Transfer 37, 139–151.

Abe, K., Kondoh, T., Nagano, Y., 1995. A new turbulence model for predicting fluid flow and heat transfer in separating and reattaching flows—ii. thermal field calculations. Int. J. Heat Mass Transfer 38, 1467–1481.

Archambeau, F., Méchitoua, N., Sakiz, M., 2004. Code Saturne: A finite volume code for the computation of turbulent incompressible flows - Industrial applications. Int. J. Finite Vol. 1.

Da Vià, R., Manservisi, S., 2019. Numerical simulation of forced and mixed convection turbulent liquid sodium flow over a vertical backward facing step with a four parameter turbulence model. Int. J. Heat Mass Transfer 135, 591–603.

Da Vià, R., Manservisi, S., Menghini, F., 2016. A k-Ω-k_θ-Ω_θ four parameter logarithmic turbulence model for liquid metals. Int. J. Heat Mass Transfer 101, 1030–1041.

De Santis, A., Shams, A., 2018. Application of an algebraic turbulent heat flux model to a backward facing step flow at low Prandtl number. Ann. Nucl. Energy 117, 32–44.

Gajetti, E., Marocco, L., Boccardo, G., Buffo, A., Savoldi, L., 2024. Implementation of a Lag Elliptic-Blending model for RANS equations in OpenFOAM. OpenFOAM® J. 4, 105–117.

Grötzbach, G., 2013. Challenges in low-Prandtl number heat transfer simulation and modelling. Nucl. Eng. Des. 264, 41–55, SI:NURETH-14.

Kawamura, H., 2004. Direct numerical simulation data base for turbulent channel flow with heat transfer. URL: https://www.rs.tus.ac.jp/t2lab/db/.

Kays, W.M., 1994. Turbulent Prandtl number - where are we? J. Heat Transf. 116, 284–295.

Kenjeres, S., Gunarjo, S.B., Hanjalić, K., 2005. Contribution to elliptic relaxation modelling of turbulent natural and mixed convection. Int. J. Heat Fluid Flow 26, 569–586.

Lardeau, S., Manceau, R., 2014. Computations of complex flow configurations using a modified elliptic-blending Reynolds-Stress model. In: 10th International ERCOFTAC Symposium on Engineering Turbulence Modelling and Measurement. Marbella, Spain, p. 8, URL: https://hal.science/hal-01051799.

Lien, F.S., Chen, W.L., Leschziner, M.A., 1996. Low-Reynolds-number eddy-viscosity modelling based on non-linear stress-strain/vorticity relations. In: Rodi, Bergeles (Eds.), Engineering Turbulence Modelling and Measurements 3. Elsevier, pp. 91–100, URL: https://doi.org/10.1016/B978-0-444-82463-9.50015-0.

Manceau, R., 2015. Recent progress in the development of the Elliptic Blending Reynolds-stress model. Int. J. Heat Fluid Flow 51, 195–220.

Manservisi, S., Menghini, F., 2014a. A CFD four parameter heat transfer turbulence model for engineering applications in heavy liquid metals. Int. J. Heat Mass Transfer 69, 312–326.

Manservisi, S., Menghini, F., 2014b. Triangular rod bundle simulations of a CFD k-ε-k_θ-ε_θ heat transfer turbulence model for heavy liquid metals. Nucl. Eng. Des. 273, 251–270.

Manservisi, S., Menghini, F., 2015. CFD simulations in heavy liquid metal flows for square lattice bare rod bundle geometries with a four parameter heat transfer turbulence model. Nucl. Eng. Des. 295, 251–260.

Marocco, L., Cammi, G., Flesch, J., Wetzel, T., 2016. Numerical analysis of a solar tower receiver tube operated with liquid metals. Int. J. Therm. Sci. 105, 22–35.

Mathur, A., Roelofs, F., Fiore, M., Koloszar, L., 2023. State-of-the-art turbulent heat flux modelling for low-prandtl flows. Nucl. Eng. Des. 406, aper no. 112241.

Menter, F.R., Kuntz, M., Langtry, R., 2003. Ten years of industrial experience with the SST turbulence model. In: Hanjalić, K., Nagano, Y., Tummers, M. (Eds.), Turbulence, Heat and Mass Transfer 4. Begell House, Inc., New York, pp. 625–632.

Niemann, M., Fröhlich, J., 2016. Buoyancy-affected backward-facing step flow with heat transfer at low Prandtl number. Int. J. Heat Mass Transfer 101, 1237–1250.

OpenCFD Ltd, 2022. OpenFOAM®. URL: https://develop.openfoam.com/Development/openfoam/-/tree/OpenFOAM-v2212.

Pope, S.B., 2000. Turbulent Flows. Cambridge University Press.

Roelofs, F., 2020. Liquid metal thermal hydraulics: State-of-the-art and future perspectives. Nucl. Eng. Des. 362, 110590.

Schumm, T., Niemann, M., Magagnato, F., Marocco, L., Frohnapfel, B., Fröhlich, J., 2015. Numerical prediction of heat transfer in liquid metal applications. In: Proceedings of the Eighth International Symposium on Turbulence Heat and Mass Transfer. pp. 263–266. http://dx.doi.org/10.1615/ICHMT.2015.THMT-15.460.

Shams, A., 2018. Towards the accurate numerical prediction of thermal hydraulic phenomena in corium pools. Ann. Nucl. Energy 117, 234–246.

Shams, A., De Santis, A., 2019. Towards the accurate prediction of the turbulent flow and heat transfer in low-Prandtl fluids. Int. J. Heat Mass Transfer 130, 290–303.

Shams, A., Roelofs, F., Baglietto, E., Lardeau, S., Kenjeres, S., 2014. Assessment and calibration of an algebraic turbulent heat flux model for low-Prandtl fluids. Int. J. Heat Mass Transfer 79, 589–601.

Siemens Digital Industries Software, 2012. Simcenter STAR-CCM+. URL: https://plm.sw.siemens.com/en-US/simcenter/fluids-thermal-simulation/star-ccm/.

Straub, S., 2023. Statistics on Turbulent Forced Convection Pipe Flow with Different Thermal Boundary Conditions for Two Prandtl Numbers (Ph.D. thesis). Karlsruhe Institute of Technology (KIT), [Database]. URL: https://doi.org/10.35097/1182.

Straub, S., Forooghi, P., Marocco, L., Wetzel, T., Vinuesa, R., Schlatter, P., Frohnapfel, B., 2019. The influence of thermal boundary conditions on turbulent forced convection pipe flow at two prandtl numbers. Int. J. Heat Mass Transfer 144, 118601.

Yap, C.R., 1987. Turbulent Heat and Momentum Transfer in Recirculating and Impinging Flows (Ph.D. thesis, Dissertation). The University of Manchester, ProQuest Dissertations Publishing, (Publikationsnummer 30279570).